Microelectronics Reliability 78 (2017) 93–99

Contents lists available at ScienceDirect

Microelectronics Reliability

journal homepage: www.elsevier.com/locate/microrel

Effects of thermal aging on Cu nanoparticle/Bi-Sn solder hybrid bonding

M. Usui [a,b,*], T. Satoh [a], H. Kimura [a], S. Tajima [a], Y. Hayashi [a], D. Setoyama [a], M. Kato [b]

[a] Toyota Central R&D Labs., Inc., 41-1, Yokomichi, Nagakute, Aichi 480-1192, Japan
[b] Department of Engineering Physics, Electronics and Mechanics, Nagoya Institute of Technology, Nagoya 466-8555, Japan

ARTICLE INFO

Article history:
Received 29 May 2017
Received in revised form 28 July 2017
Accepted 29 July 2017
Available online 11 August 2017

Keywords:
Nanoparticle bonding
Sintering
Thermal aging
Heat resistance
Oxidation

ABSTRACT

The effects of high-temperature aging on a novel hybrid bonding layer were investigated. The hybrid layer, which consisted of Cu nanoparticles and a eutectic Bi-Sn solder powder, was formed by a sintering reaction of the solid-phase Cu nanoparticles and a chemical reaction involving the liquid-phase Bi and Sn in combination. The layer was used to bond a SiC chip to a direct bonded aluminum substrate. A conventional Cu nanoparticle-based bonding layer was also prepared as a reference. Samples with these bonding layers were evaluated using the thermal aging test (225 or 250 °C, 100 h). Bonding strength and synchrotron radiation computed laminography (SRCL) measurements were performed both before and after the thermal aging test. It was observed that thermal aging greatly decreased the bonding strength of the conventional layer. In contrast, the bonding strength of the hybrid layer was reduced only slightly by the thermal aging treatment. SRCL images showed that the conventional layer exhibited numerous cracks, which acted as passages for oxidation. On the other hand, in the hybrid layer, the liquid-phase Bi and Sn densified the Cu sintering phase through the formation of an alloyed Cu-Sn phase. As a result, the hybrid layer contained fewer passages for oxidation as compared to the conventional layer and maintained its bonding strength even against thermal aging. Therefore, the hybrid layer, which is highly stable against thermal aging, will be useful for the high-temperature operation of intelligent power modules.

1. Introduction

Electric vehicles, hybrid electric vehicles, and fuel cell vehicles are attracting a lot of attention because of their low emission and high fuel efficiency [1–3]. Intelligent power modules (IPMs) are used in these vehicles to convert DC electric power into AC power. SiC devices enable operation at higher frequencies and temperatures than conventional semiconductor devices. Thus, by using SiC devices, higher output power densities can be realized in IPMs [4–6]. However, to be able to use IPMs at high temperatures, their packaging materials should show high heat resistance. Therefore, significant efforts are being devoted to the development of high-temperature bonding techniques, such as Bi or Zn soldering [7–8], transient liquid-phase bonding [9], and nanoparticle-based bonding. Of these, Ag nanoparticle-based bonding has received greater attention owing to the low sintering temperature and high electrical and thermal conductivities of these nanoparticles [10–15]. On the other hand, Cu nanoparticle-based bonding is cheaper and the bonds are more tolerant to electromigration as compared to those formed using Ag nanoparticles. Thus, Cu nanoparticles are highly attractive as a cost-effective heat-resistant material [16–23]. Recently, we proposed a hybrid bonding technique that involves the sintering of Cu nanoparticles with a Bi-Sn solder powder [24]. This technique results in improved bonding strength at elevated temperatures because of the chemical reaction that occurs during the sintering process [25]. Several methods are available for testing the reliability of the bonding in power modules, such as the thermal cycling test and the power cycling test. Among them, the high-temperature stability test is the most basic one for evaluating the performance of high-temperature modules. However, the thermal stability of hybrid bonding layers has not been studied widely. Thus, in this study, the thermal aging test was performed on the proposed hybrid bonding layer, and its performance was compared to that of a Cu nanoparticle-based bonding layer.

2. Materials and methods

2.1. Sample preparation

A SiC chip (5×5 mm^2) and a ceramic substrate (20×20 mm^2) were bonded together using Cu nanoparticles, as shown in Fig. 1. To be able to study the effects of only thermal aging on a bonding layer, the thermal strain should be low. This strain is usually caused by the temperature differences during the thermal aging. Accordingly, we chose direct-bonded aluminum (DBA, Al/AlN/Al) substrates, in which the thermal strain induced is smaller than that in direct-bonded copper (Cu/SiN/Cu) substrates [26]. The SiC chip was a Schottky barrier diode from Cree, Inc. (CPW5-1200-Z050B). Table 1 lists the sintering material

* Corresponding author at: Toyota Central R&D Labs., Inc., 41-1, Yokomichi, Nagakute, Aichi 480-1192, Japan.
E-mail address: m-usui@mosk.tytlabs.co.jp (M. Usui).

http://dx.doi.org/10.1016/j.microrel.2017.07.096
0026-2714/

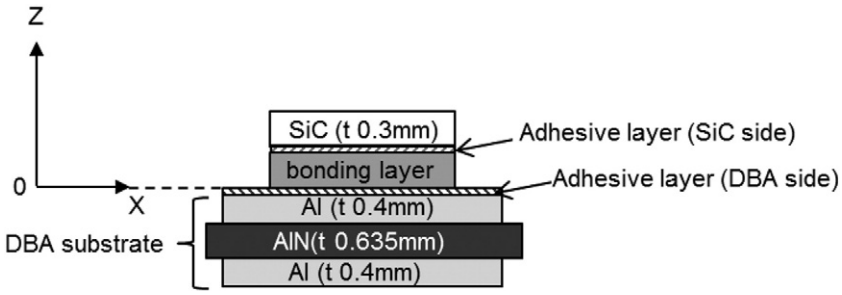

Fig. 1. Diagram illustrating layered structure of tested samples.

Table 1
Sintering material used, structure of adhesive layer, and bonding layer thickness.

Sample name	Cu nanoparticle diameter [nm]	Mixing ratio: Bi-Sn/(Bi-Sn+Cu) [weight %]	Adhesive layer [μm]		Bonding layer thickness [μm]
			SiC side	DBA side	
			Ni/Ag	Plated Ni/Ti/Ni/Ag	
Cu bonding	135	0	0.6/1.2	5/0/0.2/0.1	35
Cu-Bi-Sn bonding	230	30	0.6/1.2	0/0.1/0.2/0.1	23

used and the surface treatments performed on two types of samples tested (labeled as Cu bonding and Cu-Bi-Sn bonding). The sintering material for Cu bonding was synthesized by reducing Cu carbonate ($CuCO_3 \cdot Cu(OH)_2 \cdot H_2O$) using ethylene glycol ($HO(CH_2)_2OH$) with dodecanoic acid ($C_{11}H_{23}COOH$) and dodecyl amine ($C_{12}H_{25}NH_2$). The average diameter of the Cu nanoparticles was 135 ± 29 nm [16]. These Cu nanoparticles were selected to ensure high bonding strength at sintering temperatures lower than 350 °C [16]. The paste for Cu bonding was formed by mixing the Cu nanoparticles, α-terpineol ($C_{10}H_{17}OH$), and decanol ($C_{10}H_{21}OH$). The sintering material for Cu-Bi-Sn bonding was synthesized by reducing Cu carbonate using ethylene glycol with decanoic acid ($C_9H_{19}COOH$) and decylamine ($C_{10}H_{21}NH_2$). The diameter of the Cu nanoparticles for Cu-Bi-Sn bonding was 231 ± 78 nm [16]. The Cu nanoparticles and a eutectic Sn-43 wt% Bi (eutectic temperature of 137 °C) powder were mixed in the ratio of 7:3, and α-terpineol was added to the mixture to turn it into a paste. The diameter of the Sn-Bi particles was smaller than 38 μm. The above-described mixing conditions were used, as it has been previously reported that they are suitable for ensuring good bonding strength [24].

A Ni/Ag film was formed on the bonding surface of the SiC chip as an adhesive layer. A Ni/Ag film was also sputtered on the Ni-plated DBA substrate for Cu bonding [21,23]. A Ti/Ni/Ag film was sputtered on the DBA substrate for Cu-Bi-Sn bonding [24]. A Ti layer was used to ensure adherence between the Al and Ag/Ni layers. The thicknesses of the adhesive layers are listed in Table 1.

The samples were sintered using following process. The SiC chip was mounted on the DBA substrate after applying a 100-μm thick-layer of the nanoparticle paste on it using the bar-coating method. Next, two-step sintering (first sintering step: heating at 200 °C for 10 min; second sintering step: heating at 350 °C for 5 min) was performed on the samples in a H_2 atmosphere while applying a pressure of 0.5 MPa. The sintered samples were subjected to thermal aging in air at 1 atm. The aging treatment involved heating at 225 or 250 °C for 100 h. The thicknesses of the bonding layers are also listed in Table 1.

2.2. Characterization

Bonding strength and synchrotron radiation computed laminography (SRCL) measurements [23,27–31] were performed before and after the thermal stability test. The bonding strength test was carried out by applying a shear stress on the SiC chip at room temperature: the distance from the DBA substrate was 50 μm, and the shear rate was 50 μm/s. The average and standard deviation of the bonding strength were calculated based on the values obtained for four specimens. The fracture surfaces were observed by scanning electron microscopy (SEM).

The SRCL measurements were performed at the BL33XU Toyota beamline [32] of the SPring-8 synchrotron radiation facility. SR is characterized by high flux density, small angular divergence, and a

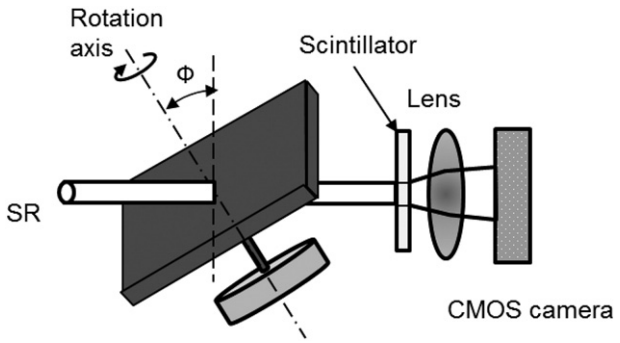

Fig. 2. Experimental setup used for SRCL observations.

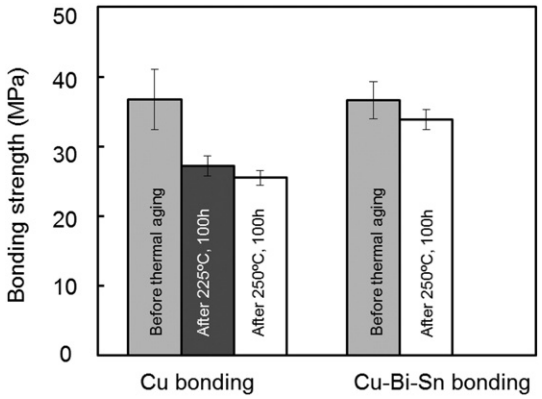

Fig. 3. Effects of thermal aging on bonding strength.

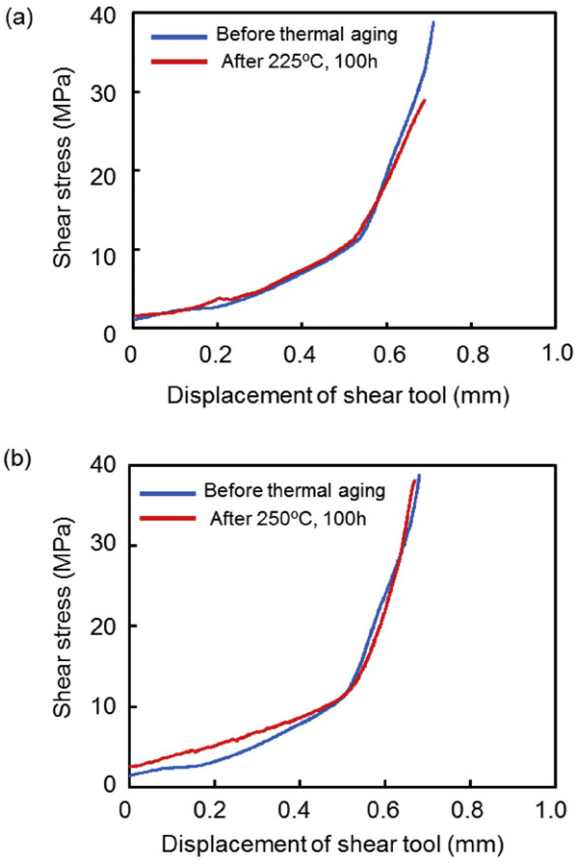

Fig. 4. Shear stress-displacement curves: (a) Cu bonding layer and (b) Cu-Bi-Sn bonding layer.

quasi-monochromatic energy spectrum that enables high-resolution analysis of various materials [33–36]. The SRCL measurement setup is shown in Fig. 2. The SR energy was 29 keV; this value was selected so that the SR beam would penetrate the samples. The rotational axis of the samples was tilted at 30° with respect to the incident beam. The exposure interval was equal to 0.1°, and the sample measurement time for one 360° rotation was ~20 min. The transmitted SR beam was converted into visible light by a scintillator, and the light was directed towards a complementary metal oxide semiconductor camera (CMOS) thorough a lens. The voxel size was 0.325 μm, and the observation area of the sample corresponded to an area with a diameter of 0.65 mm in the X-Y plane and was located at approximately the center of the bonding layer. Reconstruction was carried out by the filtered back-projection method while considering the tilt angle of the rotational axis [29]. Because of the streak artifact being parallel to the tilt angle, the quality of the reconstructed image along the X-Y plane was better than those of the images along the Y-Z and Z-X planes [29]. After the SRCL observations, the samples were mechanically polished and etched by Ar ion sputtering for cross-sectional observations. The cross-sectional images and elemental maps were obtained by SEM and energy dispersive X-ray spectrometry (EDS).

3. Results and discussion

Fig. 3 shows the effect of the thermal aging treatment on the bonding strength of the two types of specimens. Before the thermal aging treatment, the strength of the Cu bonding was similar to that of the Cu-Bi-Sn bonding. However, after the thermal aging at 225 °C and 250 °C, the strength of the Cu bonding decreased significantly, while that of the Cu-Bi-Sn bonding reduced only slightly. This high strength of the Cu-Bi-Sn bonding is consistent with our previous reports [24, 25]. Because the strength of the Cu bonding decreased significantly even after aging at the lower temperature (225 °C), we focused on the samples aged at 225 °C for the subsequent analyses.

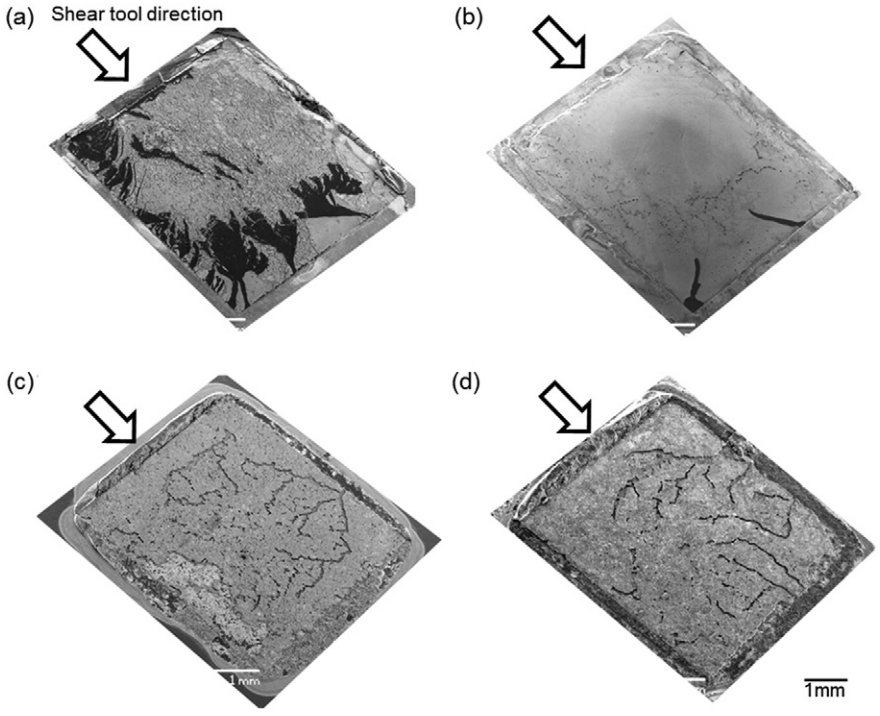

Fig. 5. SEM images of fracture surfaces: (a) Cu bonding before thermal aging, (b) Cu bonding after thermal aging, (c) Cu-Bi-Sn bonding before thermal aging, and (d) Cu-Bi-Sn bonding after thermal aging.

Fig. 4 shows shear the stress-displacement curves of the Cu bonding and Cu-Bi-Sn layers. In general, a decrease in the slope of the shear stress-displacement curve before the fracture point indicates ductile failure with plastic deformation [24,37,38]. All the curves in Fig. 4 contain only a few signs of plastic deformation, implying that brittle fracture occurred. In addition, thermal aging had little effect on the slope of the curves.

Fig. 5 shows SEM images of the fracture surfaces on the DBA substrate side. Fig. 5(a) indicates that the fracturing of the Cu bonding layer before thermal aging occurred at the bonding interface with a rough surface. Fig. 5 (b) shows that thermal aging caused the fracture surface of the Cu bonding layer to become flat, implying that brittle materials were generated at the interface [39,40]. Fig. 5(c) and (d) show that thermal aging had little effect on the flatness of the facture surface of the Cu-Bi-Sn bonding layer and that the fracture occurred at the bonding interface, where Bi was segregated [24].

Fig. 6 shows the reconstructed two-dimensional (2D) internal cross-sectional SRCL images of the Cu bonding layer before ((a), (c) and (e)) and after ((b), (d) and (f)) the thermal aging treatment. In these images, the bright areas indicate the presence of a high-density or heavy material, while the dark areas indicate the presence of a low-density or light material. Before the thermal aging process, three types of morphological features (designated as (i), (ii), and (iii) in Fig. 6(c)) were observed. Type (i) are voids with sizes of 40–100 μm. Such voids are generated by the gas molecules escaping from the solvent or the capping agent of the Cu nanoparticle paste during the sintering process. Type (ii) are cracks with widths of 1–2 μm. These cracks were caused by thermal strain arising because of the mismatch in the coefficients of thermal expansion of the SiC chip and the DBA substrate. The width of the cracks at Z = 1.0 (Fig. 6(e)) and 34.1 μm (Fig. 6(a)) is smaller than that of the cracks at Z = 17.6 μm (Fig. 6(c)). The narrow cracks near the bonding interfaces are probably attributable to the enhancement in sintering because of the large specific surface area at the interfaces. Type (iii) is a high-density sintered phase of Cu with a size of 20–80 μm. The size of this high-density phase at Z = 1.0 and 34.1 μm is smaller than that at Z = 17.6 μm. The thermal aging process shrank the voids (type (i)) and the high-density phase (type (iii)) as well as the cracks (type (ii)).

Fig. 7 shows the reconstructed 2D internal cross-sectional images of the Cu-Bi-Sn bonding layer before ((a), (c) and (e)) and after ((b), (d) and (f)) thermal aging. The thickness of the Cu-Bi-Sn bonding layer was smaller than that of the Cu bonding layer. Four types of morphological features (designated as (I)–(IV)) were observed in the Cu-Bi-

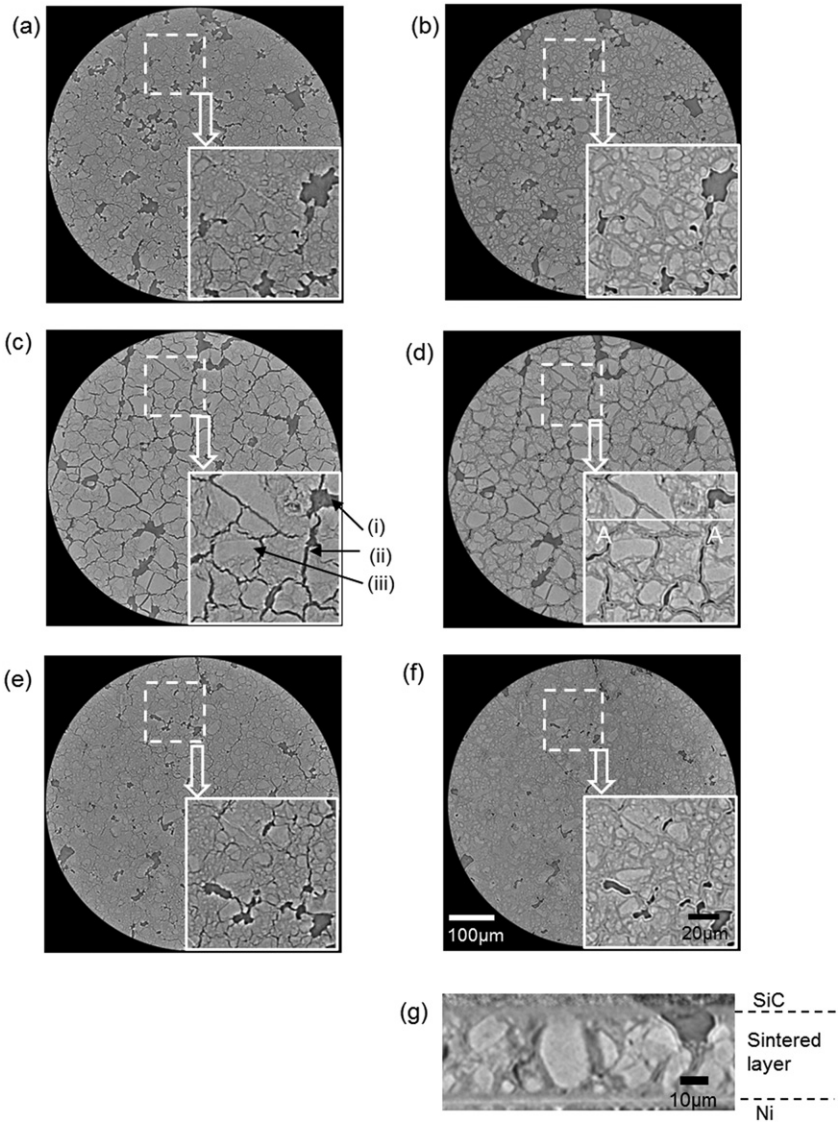

Fig. 6. Reconstructed 2D internal cross-sectional SRCL images in X − Y plane of Cu bonding layer: (a) Before thermal aging, obtained at Z = 34.1 μm, (b) after thermal aging, obtained at Z = 34.1 μm, (c) before thermal aging, obtained at Z = 17.6 μm, (d) after thermal aging, obtained at Z = 17.6 μm, (e) before thermal aging, obtained at Z = 1.0 μm, (f) after thermal aging, obtained at Z = 1.0 μm, and (g) after thermal aging, obtained in Y − Z plane at A-A cross-section.

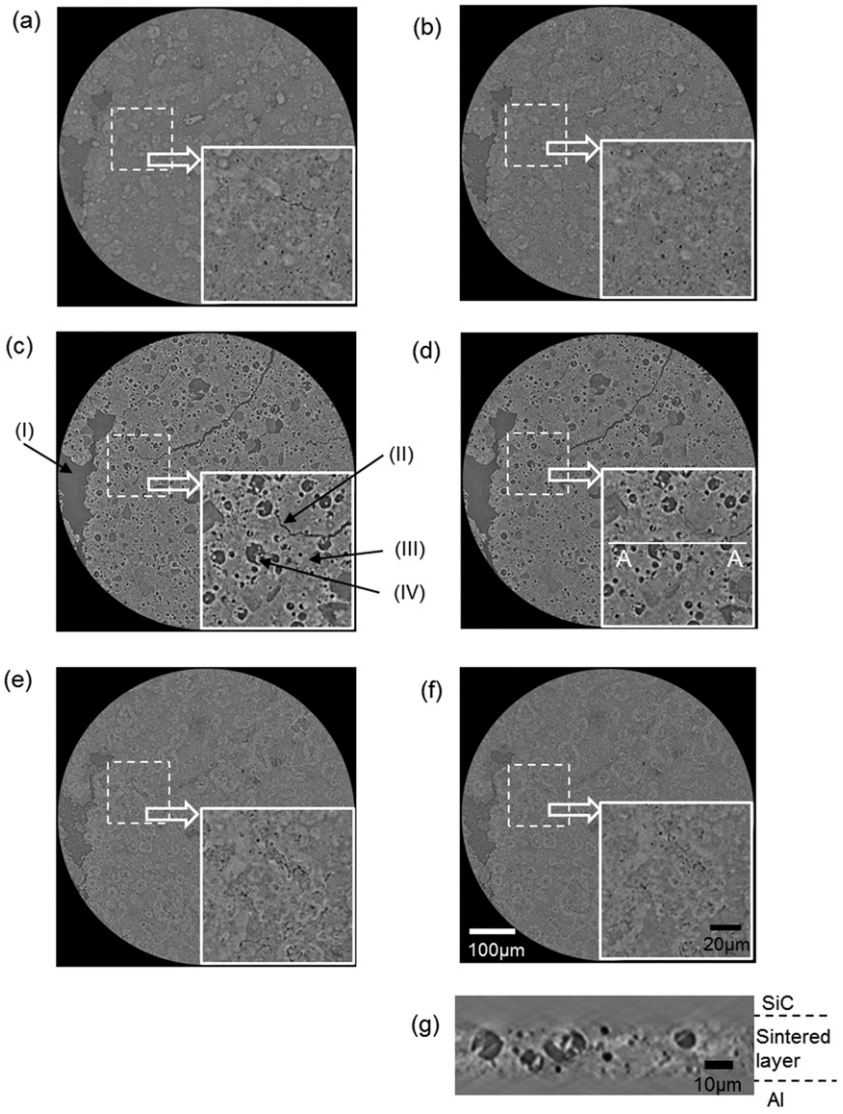

Fig. 7. Reconstructed 2D internal SRCL cross-sectional images in X—Y plane of Cu-Bi-Sn bonding layer: (a) Before thermal aging, obtained at Z = 22.1 μm, (b) after thermal aging, obtained at Z = 22.1 μm, (c) before thermal aging, obtained at Z = 11.7 μm, (d) after thermal aging, obtained at Z = 11.7 μm, (e) before thermal aging, obtained at Z = 1.0 μm, (f) after thermal aging, obtained at Z = 1.0 μm, and (g) after thermal aging, obtained in Y—Z plane at A-A cross-section.

Sn bonding layer. Type (I) are voids with sizes of 100–200 μm, which are greater than those of the voids in the Cu bonding layer. Type (II) are cracks with widths of 0.5–1 μm, which are smaller than those of the cracks in the Cu bonding layer. The number of cracks in the Cu-Bi-Sn bonding layer was much lower than the number of cracks in the Cu bonding layer. Type (III) is a high-density phase and is assumed to be a sintered Cu phase [24]. Type (IV) are voids with sizes of 10–30 μm and are considered to contain traces of the Sn-Bi powder [24]. The thermal aging treatment had little effect on the voids (type (I)), the sintered Cu phase (type (III)), or the traces of the Sn-Bi powder (type IV). Further, although the thermal aging treatment made the cracks (type II) narrower, the decrease in the width of the cracks in the Cu-Bi-Sn bonding layer was smaller than that in the width of the cracks in the Cu bonding layer. Finally, there was little change in the morphologies of both bonding interfaces (SiC chip side and DBA substrate side) because of the thermal aging treatment.

Fig. 8 shows cross-sectional SEM images of the A-A cross-section after thermal aging. The SEM images are similar to the reconstructed internal images obtained by SRCL.

Fig. 9 shows the cross-sectional SEM-EDS maps of the Cu bonding layer after thermal aging. The area with a high O signal intensity almost

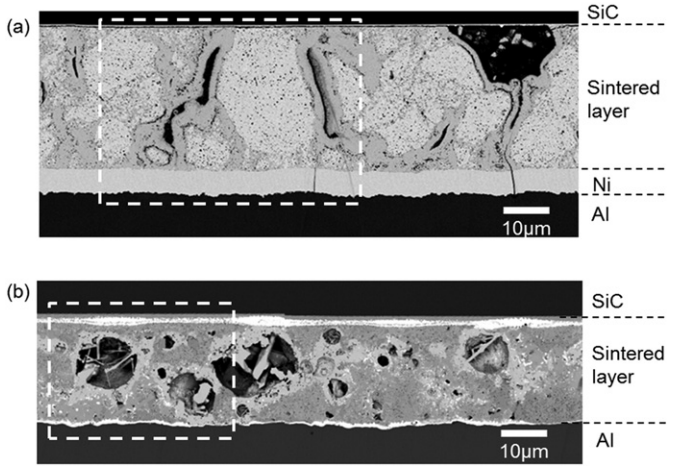

Fig. 8. Cross-sectional SEM images of A-A cross-section of bonding layer after thermal aging: (a) Cu bonding layer and (b) Cu-Bi-Sn bonding layer.

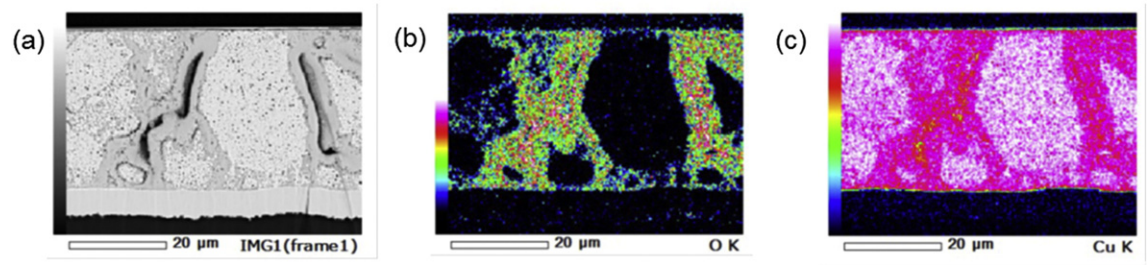

Fig. 9. Cross-sectional images of Cu bonding layer after thermal aging: (a) SEM image and SEM-EDS maps of (b) O and (c) Cu.

overlaps the area with a low Cu signal intensity. Accordingly, it is considered that the low-density Cu phase (mother phase and interfacial phase) was oxidized to a high degree.

Fig. 10 shows the cross-sectional SEM-EDS images of the Cu-Bi-Sn bonding layer after thermal aging. Four phases (A, B, C, and D) can be observed in these images. Phases A and B are high- and low-density phases of the sintered Cu mother phase. The low-density Cu with Bi phase (phase B) is oxidized to a greater degree than is the high-density Cu phase (phase A). The reason for the formation of the low-density Cu with Bi phase (phase B) is probably the low solubility of Bi in Cu [41]. Phase C mainly consists of Cu and Sn and, as per a previous report, is a Cu-Sn intermetallic compound (IMC) [24]. The sintered Cu (phases A, B) oxidized to a greater degree than did the Cu-Sn IMC (phase C). Phase D is the Bi segregated at the bonding interfaces [24]. The extent of Bi segregation on the SiC chip side is higher than that on the DBA substrate side, implying that the segregation of Bi is attributable to the thickness of the Ni layer at the interface. The Cu-Sn IMC (phase C) and the segregated Bi at the bonding interface (phase D) exhibit lower-intensity O signals compared to those of phases A and B.

It was confirmed that the addition of the Bi-Sn powder suppressed the oxidation of the Cu nanoparticle bonding layer. The reason for this improvement is as follows. Since Cu bonding is a solid-phase reaction, the sintered Cu nanoparticles do not migrate readily during the sintering-related shrinkage process, resulting in a large number of cracks (Fig. 6). These cracks act as passages for oxidation. Oxidation along these cracks causes the embrittlement of the bonding layer. In contrast, Cu-Bi-Sn bonding not only involves a solid-phase reaction but also a liquid-phase reaction. The liquid-phase Bi and Sn can migrate along the cracks during the sintering-related shrinkage process, resulting in the densification of the bonding layer, including the formation of a chemically stable alloyed Cu-Sn phase (C in Fig. 10 (a)) [9]. This causes fewer cracks compared to those in the Cu bonding layer, thus suppressing the oxidation of the bonding layer. As a result, the Cu-Bi-Sn bonding layer maintains its bonding strength even thermal aging.

The oxidation of the Cu bonding layer diminishes not only the mechanical properties but also the electric and thermal conductivities [42–45]. On the other hand, thermal stress has little effect on the properties of the Cu-Bi-Sn bonding layer. This advantage makes Cu-Bi-Sn bonding suitable for use in high-temperature power modules that need to exhibit long-term reliability.

4. Conclusions

A novel hybrid bonding layer, produced by the sintering of Cu nanoparticles with a Bi-Sn solder power, was evaluated through high-temperature aging tests. Although thermal aging greatly decreased the bonding strength of the Cu nanoparticle-based conventional bonding layer, it had little effect on the bonding strength of the hybrid layer. The SRCL results indicated that the conventional layer contained numerous cracks. These cracks were oxidized during thermal aging, resulting in a reduction in the bonding strength. In case of the hybrid layer, the liquid-phase Bi and Sn resulted in the densification of the layer. This suppressed crack generation and prevented the oxidation of the hybrid layer. As a result, the hybrid layer maintained its bonding strength even after thermal aging. These results indicated that the addition of the eutectic Bi-Sn powder improves the high-temperature stability of conventional Cu nanoparticle-based bonds.

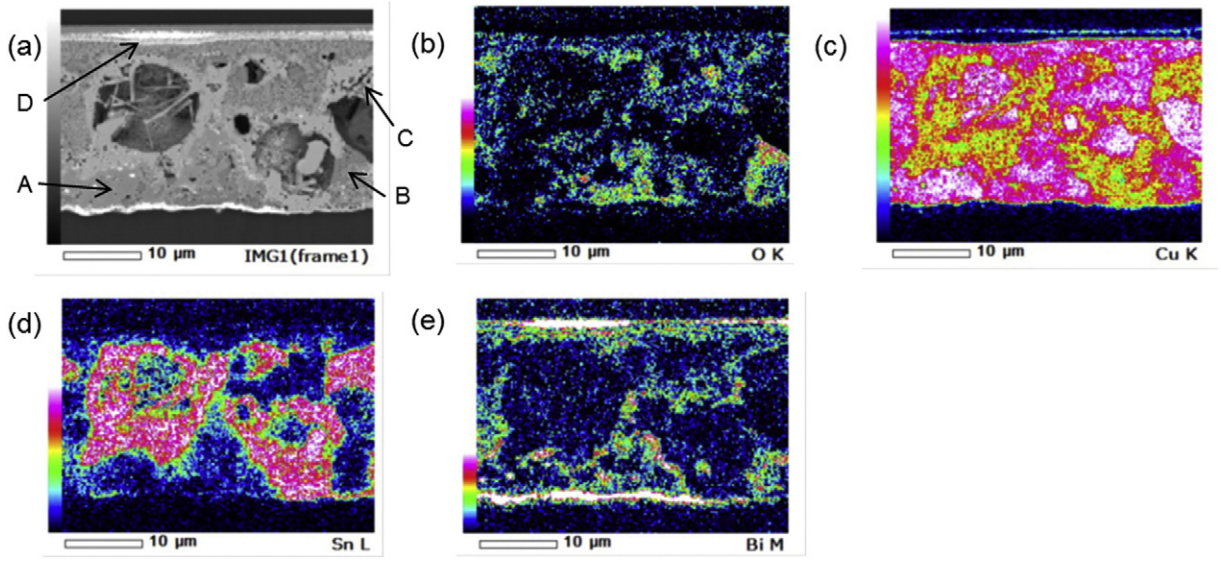

Fig. 10. Cross-sectional images of Cu-Bi-Sn bonding layer after thermal aging: (a) SEM image and SEM-EDS maps of (b) O, (c) Cu, (d) Sn, and (e) Bi.

Acknowledgements

The synchrotron radiation experiments were performed at BL33XU (Toyota beamline) of SPring-8 with the approval of the Japan Synchrotron Radiation Research Institute (JASRI) (Proposal Nos. 2016A7012 and 2016B7012). The authors would like to thank Dr. Ishizaki for technical discussions.

References

[1] H. Ohashi, I. Omura, S. Matsumoto, Y. Sato, H. Tadano, I. Ishii, Power electronics innovation with next generation advanced power devices, IEICE Trans. Comm. (2004) 3422–3429 E87-B.
[2] O. Kitazawa, T. Kikuchi, M. Nakashima, Y. Tomita, H. Kosugi, T. Kaneko, Development of power control unit for compact-class vehicle, SAE Int. J. Alt. Power. 5 (2016) 278–285.
[3] T. Hasegawa, H. Imanishi, M. Nada, Y. Ikogi, Development of the Fuel Cell System in the Mirai FCV, SAE Technical Paper 2016-01-1185, 2016.
[4] K. Hamada, M. Nagao, M. Ajioka, F. Kawai, SiC—emerging power device technology for next-generation electrically powered environmentally friendly vehicles, IEEE Trans. Electron. Devices 62 (2015) 278–285.
[5] T. Sugiura, A. Tanida, K. Tamura, Efficiency improvement of boost converter for fuel cell bus by silicon carbide diodes, SAE Int. J. Alt. Power. 5 (2016) 294–298.
[6] T. Ogawa, A. Tanida, T. Yamakawa, M. Okamura, Verification of Fuel Efficiency Improvement by Application of Highly Effective Silicon Carbide Power Semiconductor to HV Inverter, SAE Technical Paper 2016-01-1230, 2016.
[7] Y. Yamada, Y. Takaku, Y. Yagi, I. Nakagawa, T. Atsumi, M. Shirai, I. Ohmura, K. Ishida, Pb-free high temperature solder joints for power semiconductor devices, Trans. Jpn. Inst. Electron. Packag. 2 (2009) 79–84.
[8] S.-J. Kim, K.-S. Kim, S.-S. Kim, C.-Y. Kang, K. Suganuma, Characteristics of Zn–Al–Cu alloys for high temperature solder application, Mater. Trans. 49 (2008) 1531–1536.
[9] H.A. Mustain, W.D. Brown, S.S. Ang, Transient liquid phase die attach for high-temperature silicon carbide power devices, IEEE Trans. Compon. Packag. Technol. 33 (2010) 563–570.
[10] K.S. Siow, Mechanical properties of nano-silver joints as die attach materials, J. Alloy. Compd. 514 (2012) 6–19.
[11] M.-S. Kim, H. Nishikawa, Effects of bonding temperature on microstructure, fracture behavior and joint strength of Ag nanoporous bonding for high temperature die attach, Mater. Sci. Eng. A 645 (2015) 264–272.
[12] P. Quintero, P. McCluskey, B. Koene, Thermomechanical reliability of a silver nanocolloid die attach for high temperature applications, Microelectron. Reliab. 54 (2014) 220–225.
[14] S.A. Paknejad, G. Dumas, G. West, G. Lewis, S.H. Mannan, Microstructure evolution during 300 °C storage of sintered Ag nanoparticles on Ag and Au substrates, J. Alloy. Compd. 617 (2014) 994–1001.
[15] S. Sakamoto, T. Sugahara, K. Suganuma, Microstructural stability of Ag sinter joining in thermal cycling, J. Mater. Sci. Mater. Electron. 24 (2013) 1332–1340.
[16] T. Ishizaki, R. Watanabe, A new one-pot method for the synthesis of Cu nanoparticles for low temperature bonding, J. Mater. Chem. 22 (2012) 25198–25206.
[17] X. Liu, H. Nishikawa, Low-pressure Cu—Cu bonding using in-situ surface-modified microscale Cu particles for power device packaging, Script. Mater. 120 (2016) 80–84.
[18] O. Mokhtari, H. Nishikawa, Transient liquid phase bonding of Sn–Bi solder with added Cu particles, J. Mater. Sci. Mater. Electron. 27 (2016) 4232–4244.
[19] T. Satoh, K. Akedo, T. Ishizaki, X-ray photoelectron spectroscopic study of the formation of Cu/Ni interface mediated by oxide phase, J. Alloy. Comp. 582 (2014) 403–407.
[20] T. Satoh, T. Ishizaki, K. Akedo, Behavior of thin copper oxide on silver as an analogue for copper nanoparticles, J. Alloy. Comp. 691 (2017) 524–529.
[21] T. Ishizaki, M. Usui, Y. Yamada, Thermal cycle reliability of Cu-nanoparticle joint, Microelectron. Reliab. 55 (2015) 1861–1866.
[22] T. Ishizaki, D. Miura, A. Kuno, R. Nagao, S. Aoki, Y. Ohshima, T. Kino, M. Usui, Y. Yamada, Power cycle reliability of Cu nanoparticle joints with mismatched coefficients of thermal expansion, Microelectron. Reliab. 64 (2016) 287–293.
[23] M. Usui, H. Kimura, T. Satoh, T. Asada, S. Yamaguchi, M. Kato, Degradation of a sintered Cu nanoparticle layer studied by synchrotron radiation computed laminography, Microelectron. Reliab. 63 (2016) 152–158.
[24] T. Satoh, T. Ishizaki, M. Usui, Nanoparticle/solder hybrid joints for next-generation power semiconductor modules, Mater. Des. 124 (2017) 203–210.
[25] S. Tajima, T. Satoh, T. Ishizaki, M. Usui, Behavior of eutectic Sn–Bi powder in Cu nanoparticle joints during the thermal treatment, J. Mater. Sci. Mater. Electron. 28 (2007) 8764–8770.
[26] X.S. Ning, Y. Lin, W. Xu, R. Peng, H. Zhou, K. Chen, Development of a directly bonded aluminum/alumina power electronic substrate, Mater. Sci. Eng. B 99 (2003) 479–482.
[27] L. Helfen, F. Xu, H. Suhonen, P. Cloetens, T. Baumbach, Laminographic imaging using synchrotron radiation–challenges and opportunities, J. Phys. Conf. Ser. 425 (2013) 192025–192030.
[28] Y. Cheng, V. Altapova, L. Helfen, F. Xu, T.S. Rolo, P. Vagovic, M. Fiederle, T. Baumbach, Multi-contrast computed laminography at ANKA light source, J. Phys. Conf. Ser. 463 (2013) 012038–012041.
[29] H. Tsuritani, T. Sayama, Y. Okamoto, T. Takayanagi, M. Hoshino, K. Uesugi, T. Mori, Nondestructive observation of thermal fatigue crack propagation in FBGA and die attached solder joints by synchrotron radiation X-ray laminography, Proc. ASME (2015) IPACK2015－48553 (2015) V002T02A024.
[30] M. Hoshino, K. Uesugi, A. Takeuchi, Y. Suzuki, N. Yagi, Development of X-ray laminography under an X-ray microscopic condition, Rev. Sci. Instrum. 82 (2011), 073706. .
[31] T. Asada, H. Kimura, S. Yamaguchi, S. Hayashi, Y. Uyama, Measurement of 3-dimensional internal strain field in power module package by synchrotron laminography and volumetric digital image correlation method, Proc. Int. Conf. Adv. Technol. Exp. Mech. 48 (2015).
[32] T. Nonaka, K. Dohmae, Y. Hayashi, T. Araki, S. Yamaguchi, Y. Nagai, Y. Hirose, T. Tanaka, H. Kitamura, T. Uruga, H. Yamazaki, H. Yumoto, H. Ohashi, S. Goto, Toyota beamline (BL33XU) at SPring-8, AIP Conf. Proc. 1741 (2016), 030043. .
[33] L. Wang, M. Li, J. Almer, T. Bieler, R. Barabash, Microstructural characterization of polycrystalline materials by synchrotron X-rays, Front. Mater. Sci. 7 (2013) 156–169.
[34] J.J. Williams, Z. Flom, A.A. Amell, N. Chawla, X. Xiao, F. De Carlo, Damage evolution in SiC particle reinforced Al alloy matrix composites by X-ray synchrotron tomography, Acta Mater. 58 (2010) 6194–6205.
[35] Y. Hayashi, Y. Hirose, Y. Seno, Polycrystal orientation mapping using scanning three-dimensional X-ray diffraction microscopy, J. Appl. Crystallogr. 48 (2015) 1094–1101.
[36] D. Setoyama, Y. Hayashi, N. Iwata, Crystal plasticity finite element analysis based on crystal orientation mapping with three-dimensional X-ray diffraction microscopy, Mater. Sci. Forum 777 (2014) 142–147.
[37] S.S. Ha, J.K. Jang, S.O. Ha, J.W. Kim, J.W. Yoon, B.W. Kim, S.K. Park, S.B. Jung, Mechanical property evaluation of Sn-3.0A-0.5Cu BGA solder joints using high-speed ball shear test, J. Electron. Mater. 38 (2009) 2489–2495.
[38] W.H. Wu, C.S. Lin, S.H. Huang, C.E. Ho, Influence of palladium thickness on the soldering reactions between Sn-3Ag-0.5Cu and Au/Pd(P)/Ni(P) surface finish, J. Electron. Mater. 39 (2010) 2387–2396.
[39] S.W. Kim, S.B. Jung, IMC growth and shear strength of Sn-Ag-Bi-In/Au/Ni/Cu BGA joints during aging, Mater. Trans. 45 (2004) 727–733.
[40] Q.S. Zhu, Z.F. Zhang, Z.G. Wang, Inhibition of interfacial embrittlement at SnBi/Cu single crystal by electrodeposited Ag film, J. Mater. Res. 23 (2008) 78–82.
[41] B. Predel, Phase equilibria, crystallographic and thermodynamic data of binary alloys B-Ba–C-Zr, in: O. Madelung (Ed.), Landolt-Börnstein - Group IV Physical Chemistry, vol. 5B, 1992http://materials.springer.com/bp/docs/978-3-540-46733-5.
[42] B.T. Collins, W. Desisto, R. Kershaw, K. Dwight, A. Wold, Preparation and characterization of Cu(II) oxide, J. Less Common Metals 156 (1989) 341–346.
[43] L.D.L.S. Valladares, D.H. Salinas, A.B. Dominguez, D. Acosta Najarro, S.I. Khondaker, T. Mitrelias, C.H.W. Barnes, J.A. Aguiar, Y. Majima, Crystallization and electrical resistivity of Cu_2O and CuO obtained by thermal oxidation of Cu thin films on SiO_2/Si substrates, Thin Solid Films 520 (2012) 6368–6374.
[44] T. Yamakawa, T. Takemoto, M. Shimoda, H. Nishikawa, K. Shiokawa, N. Terada, Influence of joining conditions on bonding strength of joints: efficacy of low-temperature bonding using Cu nanoparticle paste, J. Electron. Mater. 42 (2013) 1260–1267.
[45] J.R. Davis, Copper and Copper Alloys, ASM International, 2010.